Optimal control of universal quantum gates in a double quantum dot

Leonardo K. Castelano,[1] Emanuel F. de Lima,[1] Justino R. Madureira,[2] Marcos H. Degani,[3] and Marcelo Z. Maialle[3,*]
[1]*Departamento de Física, Universidade Federal de São Carlos, São Carlos, SP 13565-905, Brazil*
[2]*Faculdade de Ciências Integradas do Pontal, Universidade Federal de Uberlândia, Ituiutaba, MG 38304-402, Brazil*
[3]*Faculdade de Ciências Aplicadas, Universidade Estadual de Campinas, Limeira, SP 13484-350, Brazil*

(Received 8 October 2017; revised manuscript received 23 April 2018; published 4 June 2018)

We theoretically investigate electron spin operations driven by applied electric fields in a semiconductor double quantum dot (DQD) formed in a nanowire with longitudinal potential modulated by local gating. We develop a model that describes the process of loading and unloading the DQD taking into account the overlap between the electron wave function and the leads. Such a model considers the spatial occupation and the spin Pauli blockade in a time-dependent fashion due to the highly mixed states driven by the external electric field. Moreover, we present a road map based on the quantum optimal control theory (QOCT) to find a specific electric field that performs two-qubit quantum gates on a faster timescale and with higher possible fidelity. By employing the QOCT, we demonstrate the possibility of performing within high efficiency a universal set of quantum gates {CNOT, H, and T}, where CNOT is the controlled-NOT gate, H is the Hadamard gate, and T is the $\pi/8$ gate, even in the presence of the loading/unloading process and charge noise effects. Furthermore, by varying the intensity of the applied magnetic field B, the optimized fidelity of the gates oscillates with a period inversely proportional to the gate operation time t_f. This behavior can be useful to attain higher fidelity for fast gate operations (>1 GHz) by appropriately choosing B and t_f to produce a maximum of the oscillation.

DOI: 10.1103/PhysRevB.97.235301

I. INTRODUCTION

Different proposals for quantum bits (qubits) in solid state systems have been realized [1–5]. Among them, quantum dots in semiconductors are promising candidates for quantum computation platforms due to the mature stage of the technology for semiconductor devices, including advanced growth material processing as well as the possibility of integrating structures on nanometer scales [6,7]. Essentially, the quantum dot provides spatial confinement for quantization of the electronic motion and also protects the qubit from the neighboring environment, therefore prolonging the quantum coherences. There are proposals for quantum dots using either charge [8] or spin [9,10] as qubits, or both [11], whereas spins seem to be more favorable because of their longer decoherence times due to the weaker nature of the magnetic interactions. Nonetheless, it is common to have spin decoherence caused by charge dynamics [12]. Of course, the coupling with the environment cannot be completely suppressed, as for instance in the case of the hyperfine interaction of the electron spin with nuclear spins of the host material [13], or even because the qubits have to interact externally to be controlled.

Among the proposals for semiconductor quantum dots hosting qubits [3], there is a very controllable architecture of a double quantum dot (DQD) created by local gates in semiconductor nanowires [14–16], which in turn is connected to source and drain leads [see Fig. 1(a)]. Applied voltages to the gates modify the potential profile along the nanowire, providing a versatile way of controlling the interdot tunneling as well as the electron occupation in each quantum dot. The local gates can also serve as an input for time-dependent electrical fields that, via spin-orbit coupling, act as effective magnetic fields on the electron spins [16]. In essence, these types of nanowire DQDs behave as quantum tunneling devices in which the Coulomb blockade produces very distinctive charge stability diagrams when measuring the current through the DQD [14–16]. Moreover, the current depends on the spin orientations of the unpaired electrons, an effect known as the Pauli or spin blockade [17], which is useful to access the spin configuration of two-electron states via charge current measurements.

A common procedure for manipulating the electron spin in nanowire DQDs consists of initializing the system in the spin blockade regime, i.e., assuring that the pair of electrons has parallel spins (triplet state), then applying a gate voltage to reinforce the (Coulomb) blockade [3]. In this double-blockade regime, the spin manipulation can be done by oscillating magnetic fields (electron spin resonance, ESR) or oscillating electric fields via effective magnetic field of the spin-orbit effect (electron dipole spin resonance, EDSR). The latter is technologically more attractive since it is an all-electrical technique, which can be implemented locally controlling the gate voltages. Magnetic field gradients due to implanted micromagnets are also used to attain independent control of spins occupying different dots in the DQD [4,18]. Finally, the readout is done by lifting the Coulomb blockade and checking whether the spin blockade has been lifted by the manipulation procedure. If so, the final state would be a two-electron state with antiparallel spins (singlet) and a current would flow through the nanowire DQD. This scheme implies that the spin manipulation procedure is carried out in gate voltages detuned

*marcelo.maialle@fca.unicamp.br

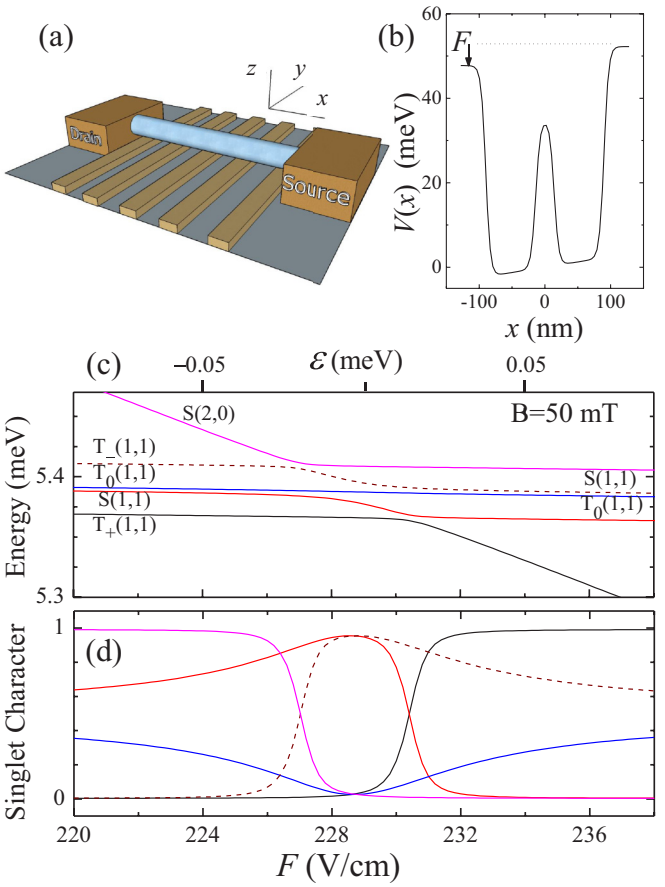

FIG. 1. (a) Schematics of the system investigated. The nanowire is connected to source and drain leads, and underneath it there are gates to modulate the electrical potential to create and control the DQD potential profile. (b) Potential profile of the DQD along the nanowire used in our calculations. The effect of an applied electric field F is shown. (c) Energy level diagram for the five lowest energy states as a function of the source-drain applied electric field F (or detuning ε). We scale $\Delta F = 100$ V/cm to $\Delta\varepsilon = 1$ meV for an average system size of 100 nm and $\varepsilon = 0$ corresponds to $F = 229$ V/cm. (d) Singlet character of the states shown in (c) as a function of the detuning. A pure singlet state has character equals 1, whereas for a pure triplet state the character is zero. Color scheme in (d) is the same as in (c).

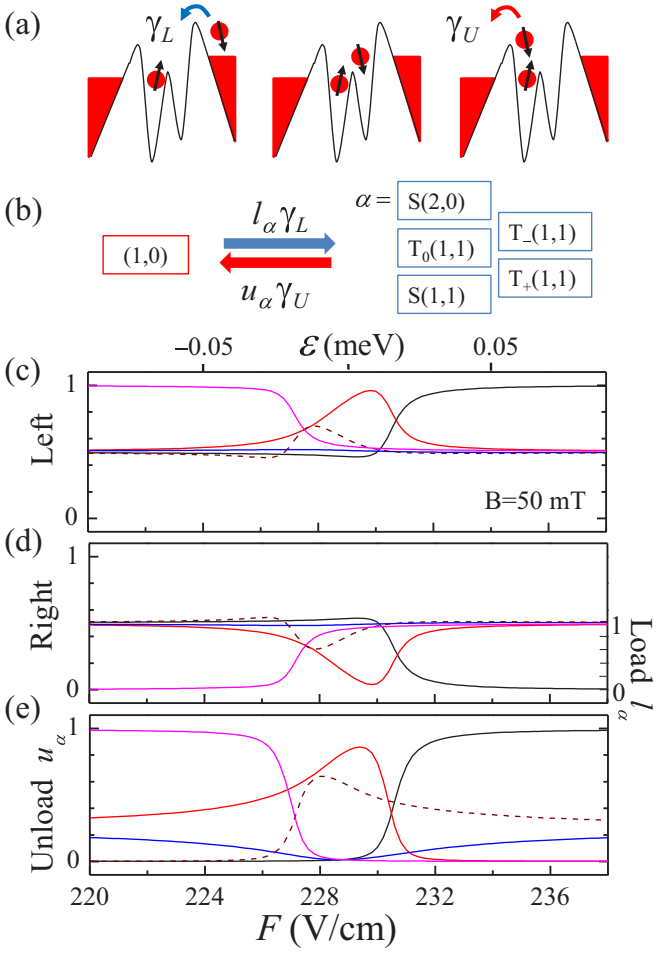

FIG. 2. (a) Schematics of the electron transfer representing the loading and unloading of the DQD. (b) Flowchart of the loading and unloading processes through the auxiliary state $|(1,0)\rangle$. Probability for finding an electron, for each eigenstate, in the (c) left and (d) right quantum dot of the DQD as function of the detuning. (d) Scale at right shows the renormalized rates for loading the DQD, l_α. (e) Unloading rates u_α as a function of the detuning. In (c)–(e), the color scheme is the same as in Fig. 1(c).

from energy level alignments (i.e., in the Coulomb blockade regime) where both ESR and EDSR need many oscillations of the applied field to accomplished the desired spin rotation.

There have been, however, alternative approaches for faster spin manipulation utilizing energy level avoided crossings [12]. If the system is forced, by a voltage change, to traverse a spin-dependent avoided crossing, the Landau-Zener (LZ) [19,20] effect can work either in favor of or in opposition to a tunneling between two energy-level avoided branches of opposite spins. This enables faster spin rotations in the spin manipulation procedure. In fact, the LZ effect was shown to produce much faster and stronger spin dynamics than the EDSR excitation, for instance, giving rise to strong resonances even for excitations with harmonic frequencies [15]. Here we investigate the LZ dynamics in a DQD and the two main contributions of this work are described in the two subsections below.

A. Fast Landau-Zener spin dynamics under charge transport cycle

LZ tunneling in a nanowire DQD introduces an adverse effect that can be prejudicial in attaining control of coherent spin dynamics. When the nanowire DQD is operated close to the two-electron avoided crossings, the singlet state [S(2,0) in Fig. 1(c)] can be populated, and since this state lifts the spin blockade and it has a strong overlap with the drain lead, it drives a charge transport through the DQD [see Figs. 2(a), 2(b)] introducing incoherent processes of the unloading and loading of the DQD. Thus, from one perspective LZ can speed up the coherent spin dynamics, but from another perspective it can lead to decoherence due to charge dynamics [12,21]. Our work investigates this situation to understand to what degree LZ tunneling can be effective in the fast manipulation of two-electron spins in nanowire DQDs.

The first main contribution of this paper is the model developed to describe the noise due to transport cycle in

this system. Our theoretical investigation starts with a model Hamiltonian [22] describing the nanowire DQD as a quasi-one-dimensional problem of two electrons (Sec. II A), in which both spatial and spin degrees of freedom are treated. This is a unique approach over the most commonly used phenomenological few-level models, and it enables us to construct a charge transport model, as discussed below. Our theoretical model has been successfully used to interpret the experimental results in Ref. [15], where it validated a simpler description by a system of a few levels [23]. In these previous works [15,23], an applied ac field forced the state to traverse rapidly the avoided crossing many times. In this situation with a very large number of LZ passages, the avoided-crossing induced decoherence and relaxation processes were approximated by transition rates taken as average constant values obtained from the experiment. The present work is a completely different case, since our goal is to investigate fast spin dynamics generated by a few LZ passages. In this case, the wave function spends a considerable portion of the operation time in the avoided-crossing region and, therefore, a better model for the transition rates is needed.

Here we present a model for the loading and unloading of the DQD, in which the transition rates depend on the spatial and spin degrees of freedom of the eigenstates. In this way, the loading/unloading rates are dependent on the source-drain applied voltage (called here *detuning* for short), which also means that time-dependent electric fields, applied to perform spin rotations, render a time dependence to the rates. This detuning/time-dependent transport cycle is important to address properly the aforementioned question about the effectiveness of LZ tunneling in the spin manipulation carried out close to the avoided crossings [21]. In summary, we use the Born-Markov approximation to describe the dissipative effects through the Lindbladian form considering rates that depend on the detuning and consequently depend on time.

B. Optimal quantum control of the spin dynamics

Another aspect of the present paper is the demonstration of the use of quantum optimal control theory (QOCT) as an efficient tool to obtain the optimized two-qubit gates in DQD systems. The progress of employing QDs as a platform for quantum computation highly depends on the accomplishment of efficient two-qubit gates in DQD systems [4]. There have been many attempts to experimentally perform two-qubit gates using DQD systems [4,24–27]. Very recently, researchers have experimentally demonstrated the controlled-NOT (CNOT) gate implementation in silicon spin qubits localized in DQDs [4]. To accomplish such a task, they have employed a magnetic field gradient together with microwave pulses and have achieved a fidelity of 80%. All pulses used in Ref. [4] are of sinusoidal type with frequencies at the resonance of the desired transition. The fidelity of quantum gates should reach values higher than 99.9% to surpass the exceeding threshold of quantum-error correction [28]. Moreover, the CNOT gate is related to the transition between states (according to the state of the first qubit), but the implementation of quantum gates that only change relative phases between states such as the $\pi/8$ gate is not easily accomplished by sinusoidal fields. Therefore, the QOCT provides a road map to obtain the quantum gate with higher fidelity on a faster timescale for each particular DQD system, thereby improving the progress of the quantum computer platform based on QDs. The QOCT has been applied to control charge populations in DQD systems [29,30], but neither the implementation of quantum gates nor the spin dynamics has been considered. Here, QOCT is invoked to design field control of spin-based operations for a universal set of quantum gates {>CNOT, H, and T}, where H is the Hadamard gate and T is the $\pi/8$ gate. We demonstrated gate control by optimal field even in the presence of strong charge transport, which otherwise could not be achieved by simpler profiles of external fields.

C. Outline

In this paper, Sec. II describes the two-electron eigenstates, their dynamical occupations, and the charge transport cycle model. Section III A shows the dynamics of two-electron states in applied pulses of electric field aiming to perform spin rotations. In Sec. III B, the optimal quantum control is used to demonstrate the feasibility of a set of universal quantum gates. Section III C contains the results including Gaussian noise effects, and Sec. III D presents the effects of varying the applied magnetic field. Section IV contains our final remarks. Appendices A and B show details of the relaxation rates introduced by the charge transport cycle. The multitarget formulation of QOCT is developed in Appendix C, and details of the system dynamics under a sinusoidal pulse are in Appendix D.

II. THEORETICAL FRAMEWORK

A. Eigenstates

We work within the effective-mass approximation considering two electrons in a nanowire as in Fig. 1(a). The Hamiltonian can be written as [22]

$$H = h_1 + h_2 + V_c(|\mathbf{r}_2 - \mathbf{r}_1|), \tag{1}$$

where V_c is the Coulomb repulsion between electrons. The single-electron Hamiltonians are

$$h_i = T_i + V(\mathbf{r}_i) + \tfrac{1}{2} g(x_i)\mu_B B\sigma_{xi} + H_{SO_i},\ i = 1,2, \tag{2}$$

with T_i being the kinetic energy operator, $V(\mathbf{r}_i)$ the structure potential, $\frac{1}{2}g(x_i)\mu_B B\sigma_{xi}$ the Zeeman term for magnetic field along the nanowire (x axis), including a position-dependent effective g factor $g(x)$ [15], and H_{SO_i} the spin-orbit interaction given below. We assume a strong confinement for the transverse directions of the nanowire, such that the electron motion can be quantized in these directions and separated from the motion along the longitudinal direction. For the transverse quantized motion, we take the ground state in a cylindrical potential and rewrite the Hamiltonian for the corresponding quasi-one-dimensional problem along the nanowire as [22]

$$H = \sum_{i=1,2}\left[-\frac{\hbar^2}{2m^*}\frac{\partial^2}{\partial x_i^2} + V(x_i) + \frac{1}{2}g(x_i)\mu_B B\sigma_{xi} + H_{SO_i}\right] + V_c(|x_1 - x_2|), \tag{3}$$

where V_c is given in Ref. [31], and the orbital effects of the magnetic field are neglected, i.e., $T_i = \frac{(\hbar \mathbf{k_i} - A_i/e^2)^2}{2m^*} \approx -\frac{\hbar^2}{2m^*}\frac{\partial^2}{\partial x_i^2}$. Again, due to the strong transverse confinement, the Rashba

spin-orbit interaction, generated by electrostatic potentials of the applied gates [32], can be approximated by [22]

$$H_{SO_i} = \alpha(\sigma_{x_i} k_{y_i} - \sigma_{y_i} k_{x_i}) \approx -\alpha \sigma_{y_i} k_{x_i}, \tag{4}$$

where α is the Rashba constant.

The Schrödinger equation is solved for the above Hamiltonian, Eqs. (3) and (4), to obtain the energies E_n and eigenstates

$$\psi_n(x_1,x_2) = \begin{bmatrix} \phi_{1n}(x_1,x_2) \\ \phi_{2n}(x_1,x_2) \\ -\phi_{2n}(x_2,x_1) \\ \phi_{3n}(x_1,x_2) \end{bmatrix} \begin{matrix} |\uparrow\uparrow\rangle \\ |\uparrow\downarrow\rangle \\ |\downarrow\uparrow\rangle \\ |\downarrow\downarrow\rangle \end{matrix} \tag{5}$$

which are written as spinors in the 1/2-spin basis $\{|\sigma_{z1}\sigma_{z2}\rangle\}$ along the z axis. The antisymmetry by the exchange of the two electrons is reinforced by the fact that the spinor components satisfy $\phi_{\rm in}(x_1,x_2) = -\phi_{\rm in}(x_2,x_1)$ for $i = 1,3$. The method for solving the Schrödinger equation was adapted from a split-operator method [33] to act in the spinor Eq. (5). This method evolves a trial wave function in imaginary time, resulting in a preferential decay of high-energy components of the trial wave functions, and is nonunitary. At each simulation step, the wave functions are normalized, orthogonality between the wave functions is ensured using a modified Gram-Schmidt method [33], and the components $\phi_{\rm in}(x_1,x_2)$ $(i = 1,3)$ of Eq. (5) are antisymmetrized. We used InAs parameters $m^* = 0.027m_0$, $\alpha = 11$ meV nm [32], and the effective g factor was taken from experiment [23], being $g(x > 0) = 6.8$ [$g(x < 0) = 7.8$] for the dot at the right (left) side of the DQD. Figure 1(b) shows the double-well confinement potential $V(x)$ along the nanowire, where the interdot potential barrier was adjusted [34] (35 meV) to produce a singlet-triplet manifold splitting of 6 meV as measured in Ref. [23].

Panel (c) of Fig. 1 shows the energies of the five lowest energy states as function of the detuning energy, $\varepsilon = -e\langle x_1 + x_2\rangle F$, due to an electric field F applied along the wire. From now on, the detuning energy ε will be used taking as reference the applied field at the anticrossing; i.e., zero detuning ($\varepsilon = 0$) means applied electric field of $F = 229$ V/cm. All results in this paper are for an applied magnetic field of $B = 50$ mT, except in Sec. III D where B is varied.

It is noticed in Fig. 1(c) that only one state has a pronounced dependence on the detuning. This state has a strong singlet character [cf. panel (d)] with two electrons on the left dot of the DQD; we denote it by S(2,0). The other four states, with weaker dependence on the detuning, have one electron in each dot: singlet S(1,1) and triplets $T_+(1,1)$, $T_0(1,1)$, and $T_-(1,1)$, where the indices $\pm,0$ give the total spin component of the state, and (n_L,n_R) gives the left and right occupations of the DQD. As the state S(2,0) approaches the (1,1) states, some avoided crossings occur. The larger avoided crossing at zero detuning, between the singlets S(2,0) and S(1,1), is due to the interdot coupling and is spin independent. The smaller avoided crossings between S(2,0) and $T_\pm(1,1)$ result from the spin-orbit interaction and they are the ones that can produce LZ spin rotations.

Not shown in the diagram of Fig. 1(c) is the triplet manifold T(2,0) which is, as mentioned, ∼6 meV higher in energy [34]. The $T_0(1,1)$ level splits from the S(1,1) away from the anticrossing region, and it wiggles around zero detuning. These effects result from the position-dependent g factor $g(x)$. It is important to stress the fact that all the states have mixed singlet-triplet characters, and this is a function of the detuning. In Fig. 1(d) we plot the singlet character of the states, defined by the degree of exchange between the particles 1 and 2. It is seen that the state S(2,0) is mostly singlet only for detunings away from zero. However, as mentioned, the position-dependent g factor mixes the singlet state S(1,1) with $T_0(1,1)$ for a broader range of detuning values, whereas the spin-orbit interaction mixes the singlet-triplet states as observed for the states S(2,0) and $T_\pm(1,1)$ in the avoided crossing regions.

We notice that similar S-T mixing could be given by the electron-nuclei spin interactions [13,35,36]. For the fast regime (∼1 ns) we want to investigate, the nuclei contribution could be considered quasistatically [36], and it has been shown [35,36] that this contribution is weaker than the spin-orbit one for relatively large B field, as it is our case of interest. This can be seen in Fig. 1(c), where the anticrossings S(2,0)-$T_\pm(1,1)$ are well apart from the anticrossing S(2,0)-S(1,1) due to large B (50 mT). Moreover, our position-dependent g factor $g(x)$ in Eq. (3) plays a role similar to that of the difference hyperfine field $\delta\mathbf{b}$ in Ref. [36]. Piezophonon [37] assisted hyperfine spin relaxation has been shown to happen for a very narrow range of values of the detuning close to $\varepsilon = 0$ [21]. This makes this process less significant than the charge dynamic dephasing, which our model accounts for by the charge transport cycle, as given below. Therefore, the level structure presented in Fig. 1(c), with spin-mixing contributions [albeit only from spin-orbit and $g(x)$, but for large B], together with the dominant dephasing due to charge transport [21], has the essential elements needed to account for the relevant spin dynamics as investigated in the following sections.

B. Dynamics under time-dependent detuning fields

In this section, we describe the time evolution of the two-electron system when subjected to time-dependent detunings. Consider that initially ($t = 0$) the system is in a given state $|\psi(t = 0)\rangle$, for instance, one of the eigenstates of Fig. 1(c) for a given detuning ε_0. If the detuning is modified, say assuming values $\varepsilon(t)$, the initial states will evolve as a mixing of the complete set of eigenstates. The dynamics can be calculated by the master equation for the density matrix $\rho(t) = |\psi(t)\rangle\langle\psi(t)|$:

$$\frac{\partial\rho}{\partial t} = \frac{1}{i\hbar}[H(t),\rho] + \mathcal{D}[\rho], \tag{6}$$

with $H(t)$ being given by Eq. (3) with the inclusion of the time-dependent applied electric field $F(t)$ along the nanowire: $V(x_i) \to V(x_i) - ex_iF(t)$, where e is the electron charge. The last right-hand-side term in Eq. (6) is the dissipator that takes into account incoherent effects as described below.

Equation (6) can be projected onto a set of eigenstates using $|\psi(t)\rangle = \sum_n a_n(t)|\psi_n\rangle$,

$$\frac{\partial\rho_{nm}}{\partial t} = \frac{1}{i\hbar}\sum_l (H_{nl}\rho_{lm} - \rho_{nl}H_{lm}) + \mathcal{D}_{nm}[\rho]. \tag{7}$$

The sum should run over a complete set of eigenstates, but in our case we approximated it by the five states calculated around zero detuning as given in Fig. 1(c). In the range around $\varepsilon = 0$, this approximation proved to be good [34]. We call

ε_0 the detuning used to project Eq. (6) in the corresponding set of states $\{|\psi_n\rangle\}$. Incoherent effects are included in Eq. (7) within the relaxation-time approximation as transition rates between different states in our vector space, and are given by the Lindblad superoperators $L[A]\rho$ (see Appendix A). While Eq. (7) is projected onto the reference set $\{|\psi_n\rangle\}$ calculated at ε_0, the incoherent state transitions have to be defined in terms of the instantaneous set $\{|\psi_\alpha\rangle\}$ calculated at the instantaneous detuning $\varepsilon(t)$. We use for the latter states Greek letter indices. The incoherent contribution to Eq. (7) reads

$$\mathcal{D}_{\alpha\beta}[\rho] = \sum_{\gamma,\delta} \Gamma_{\alpha\beta,\gamma\delta}\, \rho_{\gamma\delta}, \tag{8}$$

where $\Gamma_{\alpha\beta,\gamma\delta}$ are defined for transitions between eigenstates calculated at the instantaneous detuning $\varepsilon(t)$. Before adding Eq. (8) to Eq. (7), we must change basis $\{|\psi_\alpha\rangle\} \rightarrow \{|\psi_n\rangle\}$, yielding

$$\mathcal{D}_{nm}[\rho] = \sum_{p,k} M_{nm,pk}\, \rho_{pk}, \tag{9}$$

$$M_{nm,pk} = \sum_{\alpha,\beta,\gamma,\delta} \langle\psi_n|\psi_\alpha\rangle\langle\psi_m|\psi_\beta\rangle\Gamma_{\alpha\beta,\gamma\delta}\langle\psi_\gamma|\psi_p\rangle\langle\psi_\delta|\psi_k\rangle. \tag{10}$$

The transition rates $\Gamma_{\alpha\beta,\gamma\delta}$ are discussed in the next subsection and they are explicitly given in Appendix A.

C. Charge transport cycle

Nanowire DQD systems work as tunneling devices. The system has a charge transport cycle that loads and empties the DQD. The specific charge cycle we consider starts with only one electron in the left quantum dot, i.e., occupation (1,0) as shown in Fig. 2(a). Then, a second electron is loaded into the right quantum dot [closer to the source lead; cf. Fig. 1(a)], creating a state with occupation (1,1). This state can be either singlet, S(1,1), or triplet, $T_0(1,1)$, $T_\pm(1,1)$. The singlet has no restriction imposed by the spin blockade and it can, if energy level alignment favors, couple to the singlet S(2,0). This state, with two electrons on the left quantum dot, being closer to the drain lead, produces current and empties the DQD, returning the system to the initial occupation (1,0). On the contrary, the triplet states (1,1) are spin blocked, which allows for an initialization procedure for the two-electron system in a known spin configuration.

In this work, we construct a model for the charge transport cycle representing the loading and unloading processes described above. The model takes into account the spatial and spin degrees of freedom of the states, given by the eigenstate solutions from Sec. II A. For that, we introduce an auxiliary state representing the one-electron state $|(1,0)\rangle$ [23,38]. This state is added to the five two-electron eigenstates already discussed (see Appendix A). As mentioned above, the loading/unloading of the DQD is governed by singlet and triplet characters of the states. However, as shown in Fig. 1(d), the spin characters are functions of the detuning and, in addition, the dynamics is intended to be done under time-dependent detunings. Because of this singlet-triplet mixing, we have to ascribe rates for the loading and unloading processes connecting $|(1,0)\rangle$ to all the other five two-electron states. This is represented in Fig. 2(b), where $\gamma_{L(U)}$ is a global prefactor that is used to control the intensity of the processes and they are the only free parameters in the model. The detuning-dependent rates for each state $\{|\psi_\alpha\rangle\}$ are given by l_α and u_α as discussed next.

The eigenstates calculated in Sec. II A are used to obtain the detuning-dependent loading/unloading rates l_α/u_α. The proximity of the two-electron state to the source and drain leads is important for generating current, so we show in Figs. 2(c) and 2(d) the probabilities of finding one electron on the left and right quantum dots of the DQD, respectively. We create a rate for the loading process l_α to be proportional to the probability of the state to be closer to the source lead at the right, Fig. 2(d). Now, the probability for unloading u_α is given by the product of the probabilities of the state to be closer to the drain [Fig. 2(c)] times the singlet character of the state, given in Fig. 1(d). The latter is to ensure the lift of the spin blockade. The resulting unloading rates u_α as function of detuning are in Fig. 2(e).

Finally, the rates l_α and u_α are used to obtain $\Gamma_{\alpha\beta,\gamma\delta}$ in Eq. (8) in the instantaneous basis set $\{|\psi_\alpha\rangle\}$. We use Lindblad superoperators to take into account the incoherent contributions and the details of such a derivation are described in Appendix A. The numerical procedure used to include the detuning-dependent rates in the time evolution Eqs. (7) and (8) is given in Appendix B.

D. Multitarget optimal control

QOCT is often concerned with driving an initial known state to a desired target state by means of the shaping of an external control field [39]. There are several control algorithms to perform this goal. In particular, the control field can be efficiently designed through a monotonically convergent algorithm known as the two-point boundary-value quantum control paradigm, where the optimized control field is found interactively [40]. Of extreme relevance for quantum computing is the fact that we can formulate the QOCT problem to optimize several transitions simultaneously with the same external field. This kind of optimization is closely related to the implementation of a quantum gate, which is a unitary transformation that acts on any linear combination of the logical basis states. The key is to construct an optimized field that acts appropriately on each state of the logical basis plus a particular linear combination of all states of the logical basis. This last constraint imposed on the optimized field is necessary to avoid relative phase errors [41,42]. We refer to this approach as the multitarget optimal control algorithm and we apply this procedure to our system in order to find optimized electric fields $F(t)$ aiming at performing the set of universal quantum gates. Details of the multitarget QOCT used here are in the Appendix C.

III. RESULTS AND DISCUSSION

In this section we present the simulation results and discuss the effects of the incoherent processes due to the charge transport cycle and charge noise.

A. Spin dynamics under charge transport cycle

To illustrate the control of the spin dynamics in the nanowire DQD, we present results for applied detuning pulses which

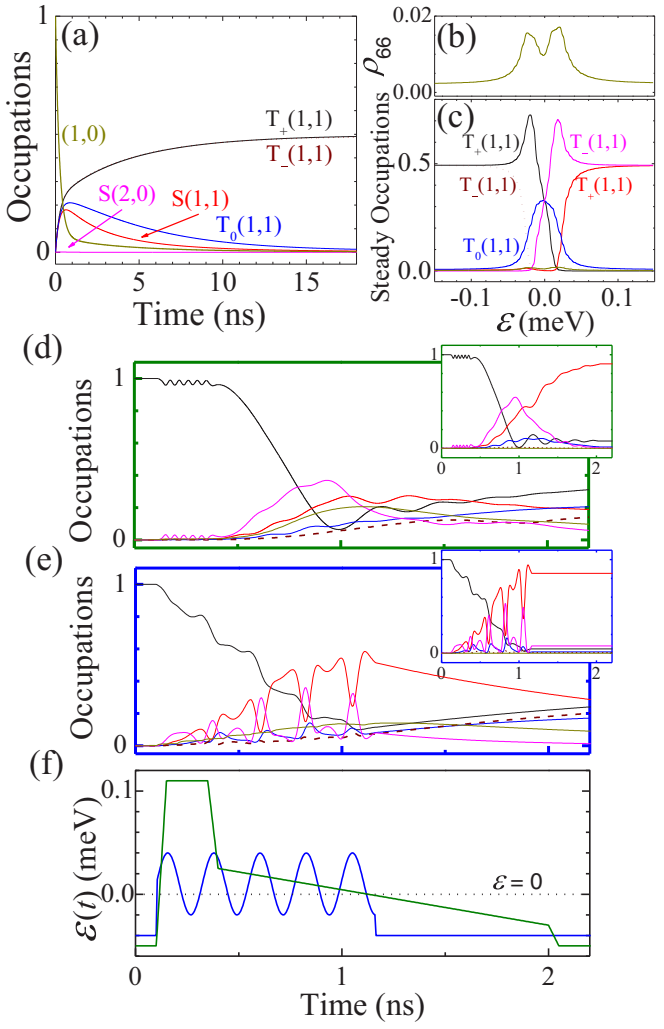

FIG. 3. (a), (b), (c) The initial state is $|(1,0)\rangle$ and the detuning is kept constant at $\varepsilon_0 = -0.09$ meV. Charge cycle rates are $\gamma_{U(L)} = 2$ GHz. (a) State occupations as function of time. (b) $|(1,0)\rangle$ occupation and (c) the other state occupations after 30 ns of simulation. (d) Simulation with a stepped detuning pulse given in (f) by the green curve. The state projections are in the eigenstate basis calculated at ε_0. The color scheme is the same as in (a). (e) Simulation with a sinusoidal pulse given in (f) by the blue curve. Insets in (d) and (e) show similar dynamics but with zero charge cycle $\gamma_{U(L)} = 0$. (f) Detuning pulse profiles as a function of time.

force the state to traverse an energy avoided crossing. In Fig. 3(a) we demonstrate the charge cycle effects, first without the detuning pulses. The system is prepared in the initial state $|(1,0)\rangle$ and the detuning remains fixed at $\varepsilon_0 = -0.09$ meV [or $F = 220$ V/cm; cf. Fig. 1(a)]. The charge cycle intensity is set as $\gamma_U = \gamma_L = 2$ GHz [15]. The evolution shows the initial state being distributed among the other two-electron states, and a stationary regime sets in with the occupation of the triplet states $T_\pm(1,1)$ being ∼50% each, all the other being close to zero. This evolution has been mentioned before as the initialization process under spin blockade, in this case without the thermalization effects, i.e., processes that favor transitions from the more energetic state to the less energetic states.

The time necessary to reach the stationary regime and the steady-state values of the triplets (1,1) depends on the detuning ε_0, as shown in Fig. 3(c), where we note a strong ε_0 dependence of the occupations around zero detuning. The reason for the unbalance between steady values of triplets (1,1) has to do with the loading/unloading rates which are detuning dependent. For instance, in the case $\varepsilon_0 \lesssim 0$, $T_-(1,1)$ mixes more with S(2,0) than $T_+(1,1)$ does; consequently for $T_-(1,1)$ the unloading rate is stronger than its (re)load rate, therefore favoring a larger steady occupation of $T_+(1,1)$. It is also interesting to note the increase of the T_0 steady occupation around zero detuning, an effect which is related to the position-dependent g factor $g(x)$. All this is consistent with the dependence of the rates on the detuning as given in Figs. 2(d) and 2(e). Figure 3(b) shows the occupation of the state $|(1,0)\rangle$ which gives a measure of the steady current through the DQD, $I \sim \gamma_L \sum_\alpha l_\alpha \rho_{66}$, where the index 6 refers to the $|(1,0)\rangle$ state. The current is more intense around zero detuning, meaning that the Coulomb and spin blockades are lifted at $\varepsilon_0 \simeq 0$ [13,35,36]. The double-humped curve reflects the fine details of the remnant spin blockade, or the triplet occupations [Fig. 3(c)], which however has not been experimentally observed [35]. One can expect this, since our model lacks additional relaxation channels [21]: (i) inelastic scattering processes, (ii) hyperfine contributions, and more importantly (iii) charge noise effects (treated in Sec. III C) that can hide the double-hump feature.

Subsequently, the initial state is driven through an avoided crossing by a detuning pulse. The initial state is now chosen to be the triplet $T_+(1,1)$ at $\varepsilon_0 = -0.05$ meV. We exemplify an attempt to make the transition $T_+(1,1) \to S(1,1)$, starting and finishing at the same detuning ε_0. The electric field pulse [Fig. 3(f), green color] has a forward ramp (increasing ε) that is faster than the return ramp. This choice is intended to control the LZ tunneling probability which depends on the speed of approaching the avoided crossing. The initial fast approaching to the avoided crossing $T_+(1,1)$-S(2,0) favors the state to remain $T_+(1,1)$, and the slow return favors the transition to S(1,1). Figure 3(d) shows the occupations $\rho_{n'n'}$ in time as seen by projections of the state on the eigenstate basis at ε_0, $\{|\psi_{n'}\rangle\}$. As expected, the forward passage through the avoided crossing kept mostly the state at $T_+(1,1)$, and the slow return enhanced the transition to the target state S(1,1) with an efficiency of ∼20% right at the end of the pulse ($t = 2$ ns). Applying the same scheme, but with zero charge cycle rates $\gamma_{U(L)} = 0$, the inset in Fig. 3(d) shows a much higher efficiency of ∼90%.

The above example of spin dynamics with detuning pulses operating at the avoided crossings shows an important aspect of the nanowire DQD system which we have already mentioned in Sec. I A. The spin dynamics is mediated by the state S(2,0), which is also the state that triggers the charge cycle and its corresponding incoherent dynamics. The slow return ramp in the pulse profile of the above example, needed to enhance the LZ transition $T_+(1,1) \to S(1,1)$, populates S(2,0). Moreover, the slow speed of this ramp makes things worse because the system stays in the strong charge cycle regime while performing the desired transition. As a result, we obtained a small efficiency for the transfer $T_+(1,1) \to S(1,1)$ when including charge cycle relaxation.

There are however means to overcome this prejudicial aspect by controlling several parameters that define the

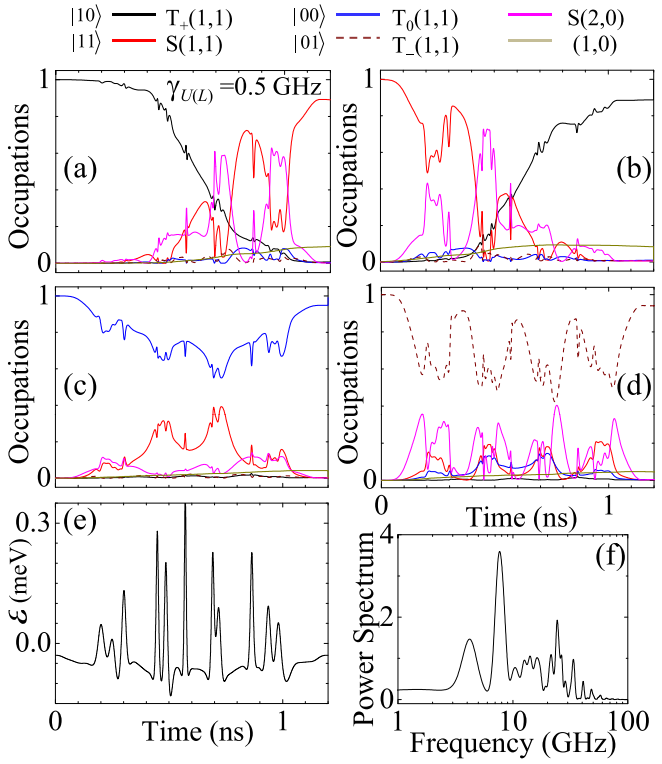

FIG. 4. Implementation of the CNOT gate. Panels (a) to (d): Occupation dynamics for the system initially prepared in states $T_+(1,1)$, $S(1,1)$, $T_0(1,1)$, and $T_-(1,1)$, respectively. (e) Optimal detuning field for the CNOT gate, and (f) corresponding power spectrum, in arbitrary units. The initial and final detuning is $\varepsilon_0 = -0.03$ meV.

dynamics of the LZ transitions. These parameters alter the phase differences between the state components when the state traverses an avoided crossing, and therefore they affect significantly the interference effects behind the LZ transition. Similarly, there is the possibility of using multiple and brief passages through the avoided crossing. This is interesting because it can have a cumulative effect. Consequently, faster detuning ramps can be repeatedly used to accomplish a desired transition, however without the nanowire DQD being subjected to the strong charge cycle for long period of times. In Fig. 3(f), the blue curve depicts a pulse profile of another attempt to perform the transition $T_+(1,1) \rightarrow S(1,1)$, starting and finishing at the same detuning ε_0. It consists of an initial very fast drive from $\varepsilon_0 = -0.04$ meV to $\varepsilon_c = 0.01$ meV, through the avoided crossing $T_+(1,1)$-$S(2,0)$, followed by five back and forth avoided crossing passages in a sinusoidal form, $\varepsilon(t) = \varepsilon_c + \varepsilon_{ac}\sin(2\pi f_0 t)$, with $\varepsilon_{ac} = 0.03$ meV and frequency ($f_0 = 4.45$ GHz) matching the energy of the transition $T_+(1,1) \rightarrow S(1,1)$ at ε_0. Finally, the detuning is returned to ε_0. In Fig. 3(e), we plot the state occupations as function of time for projections onto the eigenstate basis for ε_0. The cumulative effect is clearly seen as the initial state $T_+(1,1)$ is progressively transferred to the target state $S(1,1)$. In this case, the transfer efficiency is ∼52% (at $t = 1.2$ ns) for the charge cycle rates $\gamma_{U(L)} = 2$ GHz, and ∼86% (inset) without charge cycling, i.e., $\gamma_{U(L)} = 0$.

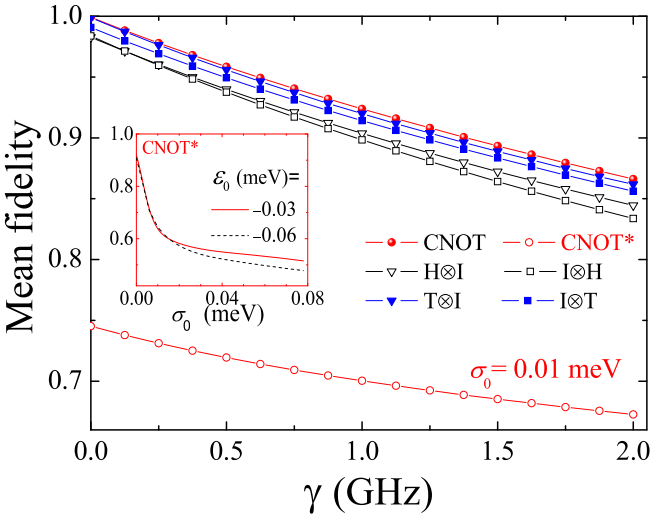

FIG. 5. Mean fidelity as a function of the charge cycle intensity ($\gamma = \gamma_L = \gamma_U$) for the universal set of quantum gates: CNOT [red solid (open) spheres without (with) the change noise effect], H ⊗ 1 (open triangles), 1 ⊗ H (open squares), T ⊗ 1 (solid triangles), and 1 ⊗ T (solid squares). All cases with detuning $\varepsilon_0 = -0.03$ meV and $t_f = 1.2$ ns. The inset shows the mean fidelity for the CNOT* gate as a function of the detuning noise spread σ_0, for $\varepsilon_0 = -0.03$ and -0.06 meV, and $\gamma = 1$ GHz.

In Appendix D we explore details of the sinusoidal excitation by varying the parameters defining its detuning pulse.

B. Implementation of quantum gates

We now turn our attention to the implementation of quantum gates. The pulse profiles we search for are now much more elaborated than the examples discussed in the previous section. So, we make use of the multitarget control algorithm (see Appendix C) to find the optimized pulses for some quantum gates. In Fig. 4 we show the results of the implementation of the controlled-NOT gate in the DQD. The CNOT gate operates on two qubits, flipping the second qubit only if the first qubit is in the state $|1\rangle$. In DQD, the qubit basis has been identified as follows: $|00\rangle \leftrightarrow T_0(1,1)$, $|01\rangle \leftrightarrow T_-(1,1)$, $|10\rangle \leftrightarrow T_+(1,1)$, and $|11\rangle \leftrightarrow S(1,1)$.

The multitarget algorithm calculations have been carried out to find the optimal electric field with the final time fixed to $t_f = 1.2$ ns and the charge cycle is omitted ($\gamma_{U(L)} = 0$) in order to keep computational times in an acceptable range. Once the optimal electrical field pulse is found [panel (e)], we turn on the charge cycle intensity to $\gamma_{U(L)} = 0.5$ GHz and calculate the occupation dynamics for the optimal field. The results are in panels (a) through (d) for the system initially prepared in states $T_+(1,1)$, $S(1,1)$, $T_0(1,1)$, and $T_-(1,1)$, respectively. It can be noticed that the gate is implemented with relatively high efficiency even under the effects of the very fast decoherent channel, as also shown in Fig. 5 for varying $\gamma_{U(L)}$. It should be emphasized that the single optimal electrical field [panel (e)] is capable of performing the CNOT gate and drives the states $|00\rangle \rightarrow |00\rangle$, $|01\rangle \rightarrow |01\rangle$, $|10\rangle \rightarrow |11\rangle$, and $|11\rangle \rightarrow |10\rangle$ with fidelity higher than 0.85, as is also shown in Fig. 5. The analysis

of the Fourier power spectrum of the optimal electrical field, shown in panel (f), reveals its frequency structure, comprising a broad frequency range up to 70 GHz. Some of the main peaks can be related to state-to-state transition frequencies. For instance, the highest peaks at around 4.2 and 7.7 GHz are close to the resonance frequencies of the $T_+(1,1) \leftrightarrow S(1,1)$ and $S(1,1) \leftrightarrow S(2,0)$ transitions, respectively. Nevertheless, such optimal field cannot be obtained by adjusting a few parameters in a guessed pulse, which emphasizes the relevance of quantum control theory in the implementation of universal quantum gates.

Furthermore, we have made an analysis of the influence of decoherence effects on the following universal set of quantum gates {>CNOT, H $\otimes$ 1, 1 $\otimes$ H, T $\otimes$ 1, and T $\otimes$ 1}, where H is the Hadamard gate, T is the $\pi/8$ gate, and 1 is the identity. In Fig. 5, we plot the mean fidelity for these gates as a function of the charge cycle intensity $\gamma = \gamma_L = \gamma_U$. A relatively small $\sim$15% decrease of the mean fidelity is observed when increasing the charge cycle frequency up to 2 GHz. The fidelity $F(\rho,\sigma) = (\mathrm{Tr}[\sqrt{\sqrt{\rho}\sigma\sqrt{\rho}}])^2$ is the measure of the distance between the density matrices ρ and σ, whereas the mean fidelity of a gate is defined as the mean of fidelities between different initial density matrices ρ_i evolved [like in panels Fig. 4(a)–;4(d)] up to the final time t_f and the density matrices obtained from the application of the gate operator $\mathcal{O}$ in the respective initial density matrices, as follows:

$$F_m = \frac{1}{5}\sum_{j=1}^{5} F(\rho_j(t_f), \mathcal{O}\rho_j), \tag{11}$$

where $\rho_1 = |00\rangle\langle 00|$, $\rho_2 = |01\rangle\langle 01|$, $\rho_3 = |10\rangle\langle 10|$, $\rho_4 = |11\rangle\langle 11|$, $\rho_5 = |\psi_5\rangle\langle\psi_5|$, where $|\psi_5\rangle = (|00\rangle + |01\rangle + |10\rangle + |11\rangle)/2$. As previously mentioned, ρ_5 is included to prevent relative phase errors that could occur when dealing separately with ρ_i, $i = 1 \ldots 4$. The pulse duration t_f and the reference detuning ε_0 are parameters that influence the effectiveness of the mean fidelity. The final time $t_f = 1.2$ ns and the reference detuning $\varepsilon_0 = -0.03$ meV maximize the mean fidelity of the CNOT gate and such parameters were used in all results of Figs. 4 and 5. The dependence on t_f is further discussed in Sec. III D.

In Fig. 6 we plot the optimal detuning fields and the corresponding power spectrum for all one-qubit gates presented in Fig. 5. Through the power spectra, one can notice the frequency decomposition signature of each gate, which has frequencies up to 100 GHz.

C. Theoretical model for the Gaussian noise

Background charge fluctuations (charge noise) is a significant issue in experimental conditions in nanowire DQDs [15]. In order to model this effect in our simulations, we assume the charge noise as slow ($< \gamma_{L(U)}^{-1}$) random sudden changes in the detuning, such that the output of many cycle measurements can be seen as an average over cycles in different detunings.

The dynamics with charge noise can be simulated by the following procedure: (i) Evaluate the dynamics given by Eqs. (6)–(10) for different values of reference detuning ε_0'. (ii) Determine the density matrix at the final state by

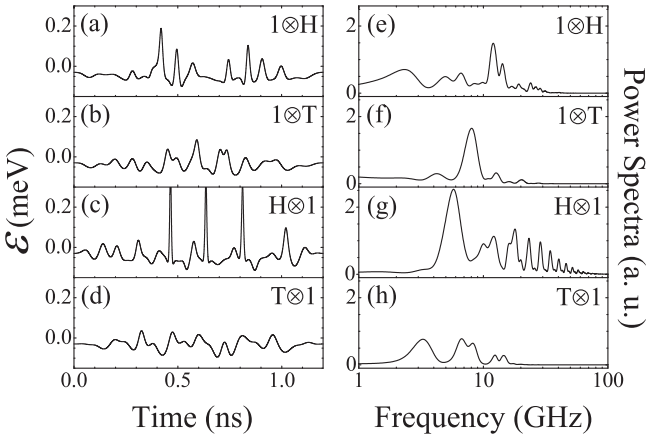

FIG. 6. Optimal detuning fields for the following one-qubit gates: 1 $\otimes$ H (a), 1 $\otimes$ T (b), H $\otimes$ 1 (c), and T $\otimes$ 1 (d). The initial and final detunings are set to $\varepsilon_0 = -0.03$ meV and $t_f = 1.2$ ns, as in Fig. 5. The corresponding power spectrum for 1 $\otimes$ H (e), 1 $\otimes$ T (f), H $\otimes$ 1 (g), and T $\otimes$ 1 (h).

considering an Gaussian average as follows:

$$\rho(\varepsilon_0, t_f) = \int d\varepsilon_0' g(\varepsilon_0', \varepsilon_0)\rho(\varepsilon_0', t_f), \tag{12}$$

where

$$g(\epsilon_0', \varepsilon_0) = \frac{1}{\sigma_0\sqrt{2\pi}} \exp\left[\frac{-(\varepsilon_0 - \varepsilon_0')^2}{2\sigma_0^2}\right], \tag{13}$$

and $\rho(\varepsilon_0', t_f)$ is the density matrix at the final time t_f, calculated for $H(\varepsilon_0')$. Finally, σ_0 gives the range of detuning variations. In Fig. 5, the charge noise effect is presented for the CNOT* gate as a function of the charge cycle intensity, with $\sigma_0 = 0.01$ meV. The inset of Fig. 5 shows the variation of the mean fidelity of the CNOT* gate as a function of the detuning spread σ_0 for a fixed value of the charge cycle intensity $\gamma = 1$ GHz and for two values of initial detuning, $\varepsilon_0 = -0.03$ and -0.06 meV. For up to $\sigma_0 \simeq 0.01$ meV, the mean fidelity decays very fast; afterwards the decay is slower. Although not shown here, we found this to be independent of ε_0 for values away from the anticrossings, $|\varepsilon_0| \gtrsim 0.02$ meV, where the qubit is usually initialized in a nonmixed spin state. Therefore, $\sigma_0 \simeq 0.01$ meV sets an upper limit for controlling the noise degradation effects in high-fidelity qubit operations.

D. Applied magnetic field

In this section, we present simulation results for varying the applied magnetic field B since this is an external parameter of the system that can be easily controlled. In our model calculation, the B-field effects can be inferred from the energy level diagram shown in Fig. 1(c). The increase of B basically increases the splitting ΔE_B between the triplets $T_\pm$ and the doublet T0-S(1,1) due to the Zeeman effect [from our numerical data: $\Delta E_B(\mathrm{meV}) \simeq 0.00043B$, with B in mT]. Also, increasing B enhances the mixing between T0 and S(1,1) due to the nonuniform g factor $g(x)$. The former effect has a direct consequence on the values of detuning ε_{SO} at which the spin-orbit avoided crossings [between $T_\pm$ and S(2,0)] take place. As the Zeeman splitting ΔE_B depends linearly on B,

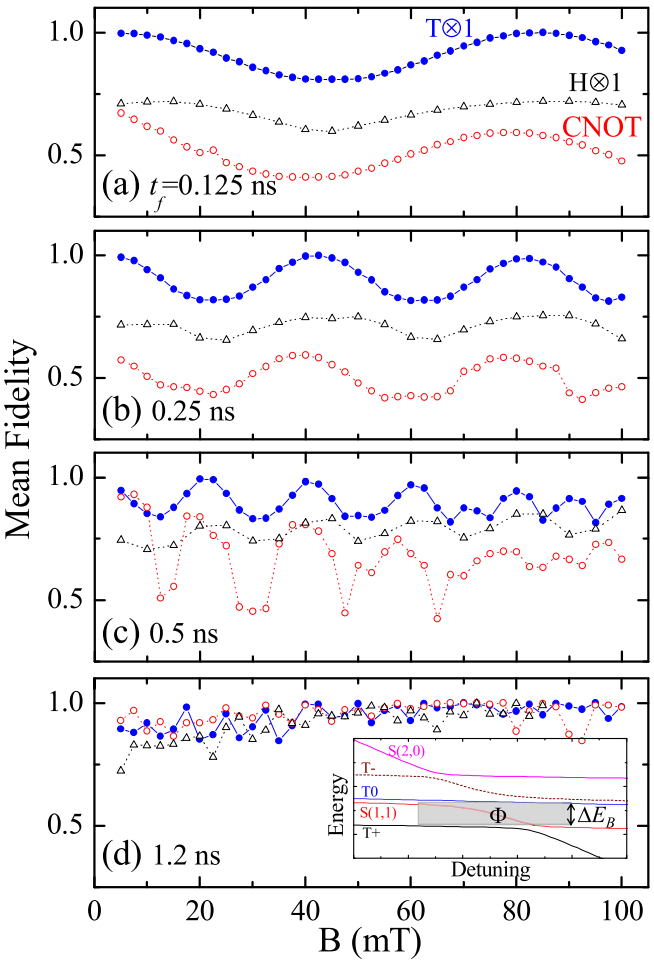

FIG. 7. Optimized mean fidelity as a function of the applied magnetic field B for the gates T ⊗ 1 (blue), H ⊗ 1 (black), and CNOT (red). The initial and final detunings are set to $\varepsilon_0 = -0.06$ meV and the final evolution time t_f is 0.125 ns (a), 0.25 ns (b), 0.5 ns (c), and 1.2 ns (d). The inset shows the energy levels as a function of detuning, as in Fig. 1(c), with the Zeeman splitting ΔE_B and schematically the phase Φ accumulated during a detuning pulse $\varepsilon(t)$.

small values of B make ε_{SO} to decrease to a point in which spin-orbit avoided crossings merge with the interdot tunneling avoided crossing ΔE_S between S(1,1) and S(2,0) (from our data, $\Delta E_S = 0.018$ meV). Equating these splittings we find that this merge occurs for $B \lesssim 40$ mT.

In Fig. 7 we present the results for the optimized mean fidelity for three quantum gates: CNOT, H ⊗ 1, and T ⊗ 1. The optimization again is done without charge cycle relaxation for the sake of reasonable computational times, although here we focus on faster gate operations ($t_f \lesssim 1$ ns) where this effect can be partially discarded. Each panel of Fig. 7 is calculated for a chosen final time t_f and the initial and final detuning values are $\varepsilon_0 = -0.06$ meV. Panel (d) is for a longer $t_f = 1.2$ ns, which is the same used in Figs. 4–6 (although for these figures $\varepsilon_0 = -0.03$ meV). Three interesting features are seen: (i) an oscillatory behavior for all gates as a function of B, with B period $\propto 1/t_f$, (ii) an increase in the mean fidelity for increasing t_f, and (iii) the simpler gates T ⊗ 1 and H ⊗ 1 resulted in higher optimized mean fidelities than the two-qubit gate CNOT, for $t_f \lesssim 1$ ns. Additionally, we have not observed any significant effect related to the merging of spin-orbit and interdot tunneling splittings (for $B \lesssim 40$ mT) as discussed above.

Features (ii) and (iii) are expected since large t_f allows the multitarget algorithm to accommodate changes in the field profile for better optimization. Feature (i) can be understood by identifying the main energy difference between the states that contributes to phase accumulation during the gate operation. This is the aforementioned Zeeman splitting ΔE_B which is approximately detuning independent [cf. inset in Fig. 7(d)]; therefore no matter the detuning values used in the pulse, this energy difference remains unchanged. During the gate operation, the state becomes a mixing of the five eigenstates (inset), and the phase accumulated Φ associated with ΔE_B, during a fixed pulse operation t_f, can have a constructive interference for $\Delta E_B t_f = 2\pi\hbar$. From this results a B period of oscillation $\propto 1/t_f$ and, for $t_f = 0.5$ ns we obtain a B period of 19.2 mT, which is in very good agreement with Fig. 7. Feature (i) is particularly important for implementing very fast gate operations (>1 GHz) because it shows that ΔE_B and t_f cannot be chosen independently if maximum fidelity is pursued.

IV. CONCLUSIONS

We have investigated the control of qubit dynamics in nanowire DQDs. The eigenstates of the system were solved for two-electron occupation in a quasi-one-dimensional model, including spin mixing via spin-orbit interaction. The eigenstates were used to construct a model for the charge transport cycle in the DQD. The transport model incorporates the spin mixing and the spatial distribution of charge in the dots. In this way, only two free parameters ($\gamma_{L(U)}$) are needed, and they control the intensity of the transport cycle. Aiming at obtaining fast spin dynamics, the simulations were performed for detunings close to the energy level avoided crossings, where charge cycle effects are more important. For simple profiles of the detuning pulse (stepped and sinusoidal), fast (∼ns) triplet-singlet transitions are possible with high efficiency as long as the singlet state S(2,0) is occupied for short times ($\gamma^{-1}_{L(U)}$).

We have also simulated the set of universal quantum gates on a very fast timescale ∼1 ns with a high fidelity, by employing the multitarget formulation of QOCT. Degradation of about 15% of the fidelity of the gate operations was observed when including fast (>1 GHz) charge cycle effects, and an additional ∼20% degradation when charge noise effects were taken into account. Nevertheless, the optimal control fields for the set of universal quantum gates have pulse profiles which can be tested in future experimental investigations. Optimized fidelity was also obtained for the gates varying the magnetic field B. For gates faster than 1 GHz, we observed an oscillatory dependence of the fidelity with B, which points out to us that the choice of B has to be related to gate operation time t_f for better efficiency of the operation. We have shown, for the particular DQD system investigated, that the QOCT is a protocol very useful to implement quantum gates, with great potential to be applied in any platform, especially those where noise has a small impact on the fidelity. If the system dynamics can be manipulated faster than all decoherent channels, such a protocol will be able to implement quantum gates with great success.

ACKNOWLEDGMENTS

The authors are grateful for financial support by the Brazilian agencies CNPq and CAPES. M.Z.M. and L.K.C. thank the support from the São Paulo Research Foundation (FAPESP), Grants No. 2017/10190-2 and No. 2012/13052-6.

APPENDIX A: MASTER EQUATION: INCOHERENT TIME EVOLUTION

The incoherent contributions to the master equation Eq. (7) are written in terms of Lindblad superoperators $L[A]\rho = A\rho A^\dagger - \frac{1}{2}(A^\dagger A\rho + \rho A^\dagger A)$. They describe the effects of the charge loading and unloading on the system in the Born-Markov approximation, where the operator A represents transitions between the one-electron state $|(1,0)\rangle$ and the two-electron states $|\psi_\alpha\rangle$, $\alpha = 1,2,\ldots,5$, and vice versa. Each transition is considered independent of each other; i.e., the loading process operator is given by $A^L_\alpha = \sqrt{\gamma_L\, l_\alpha}\,|\psi_\alpha\rangle\langle(1,0)|$ and the unloading process operator is given by $A^U_\alpha = \sqrt{\gamma_U\, u_\alpha}\,|(1,0)\rangle\langle\psi_\alpha|$, which are defined at the instantaneous detuning using the basis $\{|\psi_\alpha\rangle\}$. $\gamma_{L(U)}$ is a free parameter used to set the intensity of the charge cycle and l_α (u_α) are the rates shown in Fig. 2(d) [Fig. 2(e)] for the loading (unloading) process.

The projections of the incoherent terms of the master equation onto the reference eigenstate basis set $\{|\psi_i\rangle\}$, with the Lindblad terms in the instantaneous set $\{|\psi_\alpha\rangle\}$, read

$$\mathcal{D}_{m'n'}[\rho(t)] = \sum_{\alpha=1}^{5}\sum_{\alpha',\beta'=1}^{6}\Big\{G_{m'n',\alpha'\beta'}\left[L\left[A^L_\alpha\right]\rho\right]_{\alpha'\beta'} + G_{m'n',\alpha'\beta'}\left[L\left[A^U_\alpha\right]\rho\right]_{\alpha'\beta'}\Big\}, \tag{A1}$$

where $G_{m'n',\alpha'\beta'} = \langle\psi_{m'}|\psi_{\alpha'}\rangle\langle\psi_{\beta'}|\psi_{n'}\rangle$ and $[L[A^{L(U)}_\alpha]\rho\,]_{\alpha'\beta'} = \langle\psi_{\alpha'}|L[A^{L(U)}_\alpha]\rho\,|\psi_{\beta'}\rangle$. Here, primed indices refer to the extended basis sets including the two-electron eigenstates $\{|\psi_\alpha\rangle\}$ plus the one-electron state $|(1,0)\rangle$, i.e., $\{|\psi_{\alpha'}\rangle\} = \{\{|\psi_\alpha\rangle\},|(1,0)\rangle\}$. The state $|(1,0)\rangle$ is considered independent of the detuning, orthogonal to the other states, and shows no coherent dynamics when Eq. (7) is extended to include it, i.e., $H_{m'n'} = 0$ if either m' or $n' = |(1,0)\rangle$.

Equation (A1) can be recast in the form of Eqs. (9) and (10) with all $\Gamma_{\alpha'\beta',\gamma'\delta'}$ being zero, except those listed below:

$$\Gamma_{\alpha'\beta',\alpha'\beta'} = -\tfrac{1}{2}\,\gamma_U[u_{\alpha'} + u_{\beta'}],\ \text{for}\ \alpha'\ \text{and}\ \beta' \neq 6, \tag{A2}$$

$$\Gamma_{\alpha'6,\alpha'6} = -\tfrac{1}{2}[\gamma_L\, w + \gamma_U\, u_{\alpha'}],\ \text{for}\ \alpha' \neq 6, \tag{A3}$$

$$w = \sum_{\alpha=1}^{5} l_\alpha, \tag{A4}$$

$$\Gamma_{\alpha'\alpha',66} = \gamma_L\, l_{\alpha'},\ \text{for}\ \alpha' \neq 6, \tag{A5}$$

$$\Gamma_{6\beta',6\beta'} = -\tfrac{1}{2}[\gamma_L\, w + \gamma_U\, u_{\beta'}],\ \text{for}\ \beta' \neq 6, \tag{A6}$$

$$\Gamma_{66,\gamma'\gamma'} = \gamma_U\, u_{\gamma'},\ \text{for}\ \gamma' \neq 6, \tag{A7}$$

$$\Gamma_{66,66} = -\gamma_L\, w. \tag{A8}$$

In these equations, the index 6 refers to the $|(1,0)\rangle$ state.

APPENDIX B: DETUNING-DEPENDENT RATES: NUMERICAL PROCEDURE

Consider the system being initialized in a given detuning, which can be the one used as reference to project Eq. (7), i.e., ε_0. The initial state is chosen and written in terms of a density matrix with components projected in the reference basis $\{|\psi_{n'}\rangle\}$. When the detuning changes in time, the dynamics follows Eqs. (7) and (8), and the incoherent processes of loading/unloading of the DQD are calculated at the instantaneous basis set $\{|\psi_\alpha\rangle\}$, as discussed in Appendix A. For each change in the detuning, a transformation between basis sets $\{|\psi_\alpha\rangle\} \leftrightarrow \{|\psi_n\rangle\}$ is needed, as shown in Eq. (10). Numerically, in order to speed up the calculations, a number of basis sets for given values of detunings are previously calculated, and so are the matrices Eq. (10). As the detuning varies in time, we interpolate the instantaneous detuning to the closest one previously calculated. We have calculated a set of 150 basis sets, spanning detuning fields $F = 214$–244 V/cm, in steps of $\Delta F = 0.2$ V/cm. This range of F comprises the avoided crossings [cf. Fig. 1(a)], where the dependence on the detuning is mostly important. It is also the range of detunings in which we perform the spin dynamics under the LZ effects in this work.

APPENDIX C: MULTITARGET QOCT

Multitarget QOCT is related to the precise evolution of an initial set of states to a set of target states through the control field. The well-known variational [41] and the Krotov [42] methods have been employed to perform such a task. In this study, we employ the monotonically convergent algorithm known as the two-point boundary-value quantum control paradigm (TBQCP) [40]. We refer to this approach as the multitarget QOCT and we apply this procedure to our system in order to find the optimized electric field $F_{opt}(t)$ that performs quantum gates. The method starts with the definition of the boundary conditions, which are the set of initial states described by $\{\rho_j(0)\}$, where $j = 1,\ldots,N$ and the desired set of observables $\{O_j(t_f)\}$, at the final time t_f. Observables are evolved backwards (from the final time t_f to the initial time $t = 0$) through the following equation:

$$\frac{\partial O^{(n)}_j(t)}{\partial t} = \frac{1}{i\hbar}[H_0 - \mu F^{(n)}(t), O^{(n)}_j(t)],\quad O_j(t_f) \to O^{(n)}_j(0), \tag{C1}$$

where H_0 is the time-independent Hamiltonian of the system, μ is the dipole matrix, whose matrix elements are $\mu_{i,j} = -e\langle\psi_i(x_1,x_2)|(x_1 + x_2)|\psi_j(x_1,x_2)\rangle$, and $F^{(n)}(t)$ is the field in the nth iteration of the method. The set of initial states described by the density matrices $\{\rho_j(0)\}$ are evolved forward with the equation

$$\frac{\partial \rho^{(n+1)}_j(t)}{\partial t} = \frac{1}{i\hbar}[H_0 - \mu F^{(n+1)}(t), \rho^{(n+1)}_j(t)],\quad \rho_j(0) \to \rho^{(n+1)}_j(t_f), \tag{C2}$$

where $F^{(n+1)}(t)$ is the $(n+1)$st iteration field, which is calculated through the following expression:

$$F^{(n+1)}(t) = F^{(n)}(t) + \eta S(t) \sum_{j=1}^{N} f_j^{(n+1)}(t). \qquad \text{(C3)}$$

In Eq. (C3), η is a positive constant, $S(t)$ is a positive function, and the field correction is given by

$$f_j^{(n+1)}(t) = -\frac{1}{i\hbar}\mathrm{Tr}\{[O_j^{(n)}(t),\mu]\rho_j^{(n+1)}(t)\}. \qquad \text{(C4)}$$

Equations (C1)–(C4) are solved in a self-consistent way, starting with the trial field $F^{(0)}(t)$ and monotonically increasing the value of the desired physical observable $\langle O_j(t_f)\rangle = \mathrm{Tr}\{\rho_j(t_f)O_j(t_f)\}$. As an example, let us consider the CNOT as the quantum gate that must be implemented. In such a case, the initial set of states are $\{\rho_1(0) = |00\rangle\langle 00|, \rho_2(0) = |01\rangle\langle 01|, \rho_3(0) = |10\rangle\langle 10|, \rho_4(0) = |11\rangle\langle 11|$, and $\rho_5(0) = |\psi_5\rangle\langle\psi_5|\}$, where $|\psi_5\rangle = (|00\rangle + |01\rangle + |10\rangle + |11\rangle)/2$. The last state described by ρ_5 is included to prevent relative phase errors. The set of target observables is respectively given by $\{O_1(t_f) = |00\rangle\langle 00|, O_2(t_f) = |01\rangle\langle 01|, O_3(t_f) = |11\rangle\langle 11|, O_4(t_f) = |10\rangle\langle 10|$, and $O_5(t_f) = |\psi_5\rangle\langle\psi_5|\}$. In all numerical calculations, we have used the following parameters: $\eta = 0.0005$, $S(t) = \sin^2(\pi\, t/t_f)$, $F^{(0)}(t) = 0.035$ V/cm, and run 4000 iterations of the multitarget QOCT.

APPENDIX D: DETAILS OF THE SINUSOIDAL PULSE EXCITATION

The sinusoidal excitation has a detuning pulse given by $\varepsilon(t) = \varepsilon_c + \varepsilon_{\mathrm{ac}}\sin(2\pi f t)$. Some results were presented in Figs. 3(e) and 3(f); now we discuss the results in Fig. 8 varying $\varepsilon_{\mathrm{ac}}, \varepsilon_c$, and f. Panel (a) shows the final occupations as a function of the amplitude of the applied pulse $\varepsilon_{\mathrm{ac}}$, in which an oscillatory behavior is observed with a maximum S(1,1) transfer at $\varepsilon_{\mathrm{ac}} = 0.03$ meV, as used for Fig. 3(e). Panel (b) shows the effects of varying both the amplitude $\varepsilon_{\mathrm{ac}}$ and the center of oscillation ε_c. Again, oscillatory behavior due to interference effects of the LZ transition can be seen. In particular, very small S(1,1) transfer is achieved if $|\varepsilon_c| > \varepsilon_{\mathrm{ac}}$, that is, if the avoided crossing is not reached during the ac pulse. This gives a V-shaped pattern in Fig. 8(b). Both panels (a) and (b) were obtained for zero charge cycle, $\gamma_{U(L)} = 0$, in order to enhance the observed effects. When the charge cycle is included, the occupation transfers decrease. This can be seen in panels (c) and (d), where the frequency of the ac pulse was varied with respect to the resonant frequency of the transition $\mathrm{T}_+(1,1) \rightarrow \mathrm{S}(1,1)$ at $\varepsilon_0 = -0.04$ meV. At resonance $f = f_0 = 4.45$ GHz, a strong S(1,1) transfer is observed. For a little higher frequency $f/f_0 = 1.22$, similar resonant transfer occurs for $\mathrm{T}_+(1,1) \rightarrow \mathrm{T}_0(1,1)$, consistent with the alignment

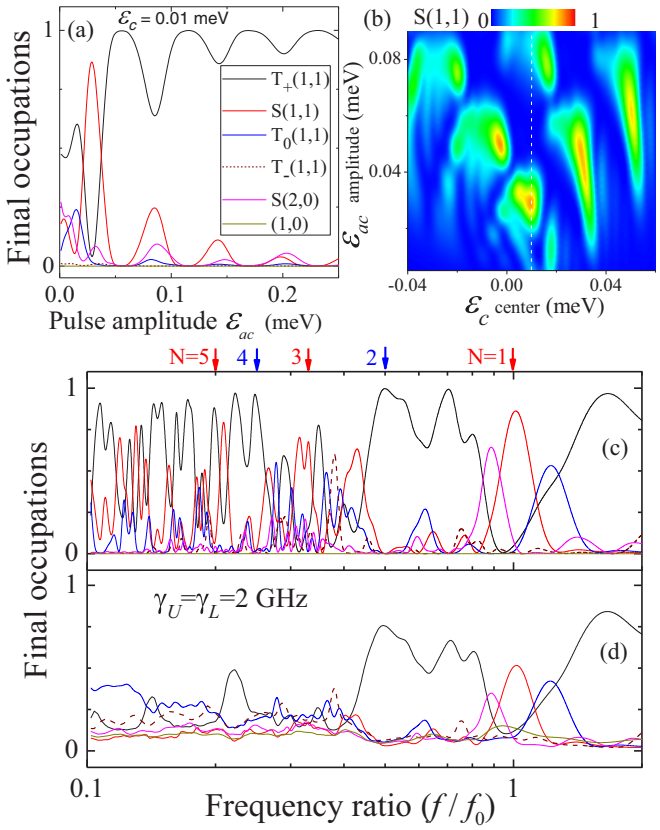

FIG. 8. Results for sinusoidal pulses similar to Fig. 3(f), $\varepsilon(t) = \varepsilon_c + \varepsilon_{\mathrm{ac}}\sin(2\pi f t)$, where f is a frequency close to the resonant frequency f_0, i.e., $hf_0 = E_{S(1,1)} - E_{T_+}$ at $\varepsilon_0 = -0.04$ meV ($f_0 = 4.45$ GHz). (a) State occupations, after 5 oscillations, as function of the detuning pulse amplitude $\varepsilon_{\mathrm{ac}}$ and with $\varepsilon_c = 0.01$ meV. (b) S(1,1) occupation after five oscillations of the sinusoidal pulse as function of $\varepsilon_{\mathrm{ac}}$ and ε_c. The vertical dashed line corresponds to the scan given in (a). (c) Final occupations after five oscillations of the sinusoidal pulse as function of the pulse frequency f in respect to f_0 (in log scale), with $(\varepsilon_0, \varepsilon_c, \varepsilon_{\mathrm{ac}}) = (-0.04, 0.01, 0.03)$ meV. (a), (b), and (c) are calculated with zero charge cycle $\gamma_{U(L)} = 0$. (d) The same as in (c) but with $\gamma_{U(L)} = 2$ GHz. The color scheme in (a) applies also to (c) and (d). Colored arrows indicate some harmonic excitations of the $\mathrm{T}_+(1,1) \rightarrow \mathrm{S}(1,1)$ transition.

of the energy levels [Fig. 1(c)]. For $f/f_0 < 1$, a large number of resonance peaks is seen, which is mostly due to the harmonic excitation of the interlevel transitions. As measured [15] and simulated [23,43], odd (even) harmonics at $\varepsilon_c \simeq 0$ enhance (deplete) the interlevel transfer, as pointed by the red (blue) arrows in Fig. 8(c) for the S(1,1) transfer. The inclusion of the charge transport cycle, panel (d), retains the effects but in a less pronounced way, especially for lower frequencies, for which longer times of simulations are needed in order to maintain fixed the 5 oscillations in the pulse, therefore favoring the action of charge cycle relaxation.

[1] J. Clarke and F. K. Wilhelm, Nature (London) **453**, 1031 (2008).
[2] L. Childress and R. Hanson, MRS Bull. **38**, 134 (2013).
[3] R. Hanson, L. P. Kouwenhoven, J. R. Petta, S. Tarucha, and L. M. K. Vandersypen, Rev. Mod. Phys. **79**, 1217 (2007).

[4] D. M. Zajac, A. J. Sigillito, M. Russ, F. Borjans, J. M. Taylor, G. Burkard, and J. R. Petta, Science **359**, 439 (2018).

[5] M. Veldhorst, J. C. C. Hwang, C. H. Yang, A. W. Leenstra, B. de Ronde, J. P. Dehollain, J. T. Muhonen, F. E. Hudson, K. M. Itoh, A. Morello, and A. S. Dzurak, Nat. Nanotechnol. **9**, 981 (2014).

[6] D. M. Zajac, T. M. Hazard, X. Mi, E. Nielsen, and J. R. Petta, Phys. Rev. Applied **6**, 054013 (2016).

[7] M. Veldhorst, H. G. J. Eenink, C. H. Yang, and A. S. Dzurak, Nat. Commun. **8**, 1766 (2017).

[8] J. Gorman, D. G. Hasko, and D. A. Williams, Phys. Rev. Lett. **95**, 090502 (2005).

[9] M. Atatüre, J. Dreiser, A. Badolato, A. Högele, K. Karrai, and A. Imamoglu, Science **312**, 551 (2006).

[10] J. R. Petta, A. C. Johnson, J. M. Taylor, E. A. Laird, A. Yacoby, M. D. Lukin, C. M. Marcus, M. P. Hanson, and A. C. Gossard, Science **309**, 2180 (2005).

[11] Z. Shi, C. B. Simmons, J. R. Prance, J. K. Gamble, T. S. Koh, Y.-P. Shim, Xuedong Hu, D. E. Savage, M. G. Lagally, M. A. Eriksson, Mark Friesen, and S. N. Coppersmith, Phys. Rev. Lett. **108**, 140503 (2012).

[12] H. Ribeiro, G. Burkard, J. R. Petta, H. Lu, and A. C. Gossard, Phys. Rev. Lett. **110**, 086804 (2013).

[13] F. H. L. Koppens, J. A. Folk, J. M. Elzerman, R. Hanson, L. H. W. v. Beveren, I. T. Vink, H. P. Tranitz, W. Wegscheider, L. P. Kouwenhoven, and L. M. K. Vandersypen, Science **309**, 1346 (2005).

[14] S. De Franceschi, J. A. van Dam, E. P. A. M. Bakkers, L. F. Feiner, L. Gurevich, and L. P. Kouwenhoven, Appl. Phys. Lett. **83**, 344 (2003).

[15] J. Stehlik, M. D. Schroer, M. Z. Maialle, M. H. Degani, and J. R. Petta, Phys. Rev. Lett. **112**, 227601 (2014).

[16] S. Nadj-Perge, S. M. Frolov, E. P. A. M. Bakkers, and L. P. Kouwenhoven, Nature (London) **468**, 1084 (2010).

[17] K. Ono, D. G. Austing, Y. Tokura, and S. Tarucha, Science **297**, 1313 (2002).

[18] M. Pioro-Ladriere, T. Obata, Y. Tokura, Y.-S. Shin, T. Kubo, K. Yoshida, T. Taniyama, and S. Tarucha, Nat. Phys. **4**, 776 (2008).

[19] L. D. Landau, Phys. Z. Sowjetunion **2**(46), 1 (1932).

[20] C. Zener, Proc. R. Soc. A **137**, 696 (1932).

[21] H. Ribeiro, J. R. Petta, and Guido Burkard, Phys. Rev. B **87**, 235318 (2013).

[22] M. P. Nowak, B. Szafran, and F. M. Peeters, Phys. Rev. B **86**, 125428 (2012).

[23] J. Stehlik, M. Z. Maialle, M. H. Degani, and J. R. Petta, Phys. Rev. B **94**, 075307 (2016).

[24] K. C. Nowack, M. Shafiei, M. Laforest, G. E. D. K. Prawiroatmodjo, L. R. Schreiber, C. Reichl, W. Wegscheider, and L. M. K. Vandersypen, Science **333**, 1269 (2011).

[25] R. Brunner, Y. S. Shin, T. Obata, M. Pioro-Ladriere, T. Kubo, K. Yoshida, T. Taniyama, Y. Tokura, and S. Tarucha, Phys. Rev. Lett. **107**, 146801 (2011).

[26] M. D. Shulman, O. E. Dial, S. P. Harvey, H. Bluhm, V. Umansky, and A. Yacoby, Science **336**, 202 (2012).

[27] M. Veldhorst, C. H. Yang, J. C. C. Hwang, W. Huang, J. P. Dehollain, J. T. Muhonen, S. Simmons, A. Laucht, F. E. Hudson, K. M. Itoh, A. Morello, and A. S. Dzurak, Nature (London) **526**, 410 (2015).

[28] D. Lidar and T. Brun, *Quantum Error Correction* (Cambridge University Press, Cambridge, UK, 2013).

[29] S. G. Kosionis, A. F. Terzis, and E. Paspalakis, Phys. Rev. B **75**, 193305 (2007).

[30] E. Räsänen, A. Putaja, and Y. Mardoukhi, Cent. Eur. J. Phys. **11**, 1066 (2013).

[31] S. Bednarek, B. Szafran, T. Chwiej, and J. Adamowski, Phys. Rev. B **68**, 045328 (2003).

[32] D. Liang and X. P. Gao, Nano Lett. **12**, 3263 (2012).

[33] M. H. Degani and M. Z. Maialle, J. Comput. Theor. Nanosci. **7**, 454 (2010).

[34] We have solved the problem for 9 states and observed the (2,0)-triplet manifold ∼6 meV higher in energy than the S(2,0) state.

[35] S. Nadj-Perge, S. M. Frolov, J. W. W. van Tilburg, J. Danon, Y. V. Nazarov, R. Algra, E. P. A. M. Bakkers, and L. P. Kouwenhoven, Phys. Rev. B **81**, 201305 (2010).

[36] D. Stepanenko, M. Rudner, B. I. Halperin, and D. Loss, Phys. Rev. B **85**, 075416 (2012).

[37] C. Weber, A. Fuhrer, C. Fasth, G. Lindwall, L. Samuelson, and A. Wacker, Phys. Rev. Lett. **104**, 036801 (2010).

[38] J. Danon and Y. V. Nazarov, Phys. Rev. B **80**, 041301(R) (2009).

[39] C. Brif, R. Chakrabarti, and H. Rabitz, New J. Phys. **12**, 075008 (2010).

[40] T.-S. Ho and H. Rabitz, Phys. Rev. E **82**, 026703 (2010).

[41] C. M. Tesch and R. de Vivie-Riedle, J. Chem. Phys. **121**, 12158 (2004).

[42] J. P. Palao and R. Kosloff, Phys. Rev. A **68**, 062308 (2003).

[43] J. Danon and M. S. Rudner, Phys. Rev. Lett. **113**, 247002 (2014).